

# Thermoelectric modeling of the ATLAS ITk Strip Detector

Kurt Brendlinger<sup>1</sup>, Georg Viehhauser<sup>1</sup>, Graham Beck<sup>1</sup>, Yu-Heng Chen<sup>1</sup>

## Abstract

Here is the abstract.

*Keywords:* Silicon detector, Thermal runaway, Thermal management, Cooling

## 1. Introduction

The temperatures in silicon detector systems are critically important for the performance of these systems.

The leakage current shows a pronounced temperature dependence

$$I \propto T_S^2 e^{-T_A/T_S}, \quad (1)$$

where  $T_S$  is the sensor temperature and  $T_A \simeq 7000$  K. Leakage currents can become particularly significant after irradiation of the silicon material. The heat generated by these leakage currents in the silicon sensor, together with the heat from front-end electronic components on the detector, needs to be removed by a cooling system. Due to the strong growth of leakage power with temperature there is a critical temperature  $T_{\text{crit}}$  above which the heat cannot be removed quickly enough, and the detector becomes thermally unstable ('thermal runaway')<sup>1</sup>. The capability of the cooling system to remove this heat is limited by the temperature of the local cold sink (typically a circulated fluid) and the thermal impedance of the heat path between the source (electronics and sensor) and the sink.

In addition, there can be aspects of the front-end electronics that are temperature-dependent. For example, in the strip system for the ATLAS Phase-II upgrade [1] there are two additional temperature-dependent heat sources. The first is a radiation damage effect in the digital part of the readout electronics (the ABC130 and HCC chips), which is manufactured in 130 nm technology by the CMOS 8RF process (ref). This effect leads to an increase of the digital power in the chip depending on the total ionisation dose (TID) and the temperature of the chip (ref). This has been first observed in the ATLAS IBL [2]. The other temperature dependence of the power generated by the front-end electronics stems from the converter chip (FEAST (ref)) used in the on-detector DC-DC converter system supplying power to the front-end electronics.

Even before the limit of thermal stability is reached, knowledge of temperatures in silicon detector systems is important, as they define system parameters like power supply capacity and cable dimensions.

In principle the temperatures in the system for a given set of operational parameters (power density, thermal conductivities, etc.) can be predicted by FEA to an accuracy that is limited only by the quality of the input parameters. However, this is a time-consuming process and can be prohibitively difficult if a number of local heat sources depend non-linearly on the temperature. A simplification to this problem that allows for an analytical solution in the case of a simple heat source topology has been developed in [3]. Here we develop this method further to include several temperature-dependent non-linear heat sources in the front-end electronics. The resulting set of equations cannot be solved analytically anymore, but the solution can be found with little effort using numerical problem solvers. This enables us to predict with some confidence the temperatures and power requirements in the ATLAS strip system throughout Phase-II operation. The results from this prediction have been used throughout the project to consistently dimension the different systems (cooling, power, services, etc.) also with some robustness due to the inclusion of a common set of

<sup>1</sup>In a real detector system the resulting growth of sensor temperature would be arrested by overcurrent limits in the power supplies, resulting in a reduction of the bias voltage. At the same time the increased current leads to an increase of the noise, so that the overall result is a degradation of the S/N performance of the system.

37 safety factors. This method can be easily adapted to any other system by adjusting to the system-specific  
38 geometries and parameters.

39 *1.1. The ATLAS strip system*

40 The strip system for the ATLAS Phase-II upgrade [1] consists of two parts: the barrel system comprises  
41 four concentric cylindrical barrels, and the two endcaps, which consist of six disks each.

42 In the barrel, the detector modules are made of square sensors ( $96.85 \times 96.72 \text{ mm}^2$ ) with a hybrid on  
43 top, which hosts the front-end chips (ABC130 and HCC), but also circuitry to convert the supply voltage of  
44 larger than 10 V to the chip voltage of 1.5 V. This circuitry is controlled by the FEAST chip. The modules  
45 are glued onto both sides of a composite sandwich that contains two parallel thin-wall titanium cooling  
46 pipes embedded in carbon foam (Allcomp K9 - ref) between two facesheets of UHM carbon fibre (3 layers  
47 of K13C2U/EX1515) with a co-cured Kapton/copper low-mass tape. A model of this geometry is shown  
48 in Fig. 1. During final operation, cooling will be achieved by evaporating CO<sub>2</sub> in the cooling pipes with a  
49 final target temperature no higher than  $-35^\circ\text{C}$  anywhere on the stave. The geometry of the stave is uniform  
50 along its length, with the exception of the end region of the stave, where an End-Of-Structure (EOS) card is  
51 mounted on both surfaces, which shares part of the heat path from the module, and where the thermal path  
52 is degraded by the presence of electrically-insulating ceramic pipe sections.

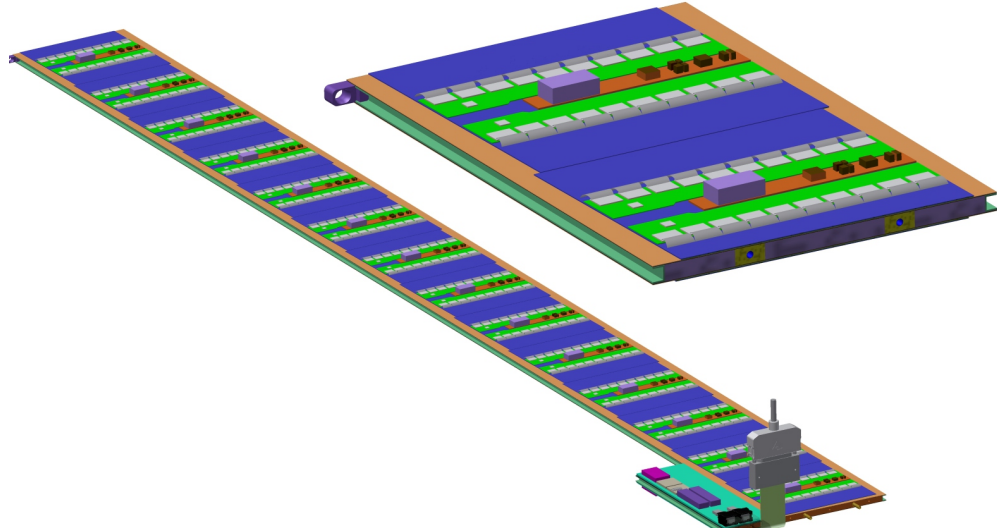


Figure 1: Strip barrel local support geometry. On the left, a complete stave is shown (EOS card in the foreground). The right picture shows a cross-section of the stave with the two cooling pipes visible inside the core.

53 The endcap detector consists of six disks, each containing 32 ‘petals’ loaded on both sides with six silicon  
54 modules (twelve in total). The endcap detector modules consist of six distinct designs located at increasing  
55 radius from the beam pipe and labeled R0 through R5 (where ‘R’ stands for ring). Each endcap module  
56 consists of one or two irregularly-shaped silicon sensors, and a varying number of front-end chips on each  
57 module (between 12 and 28 ABCs, and 2 to 4 HCCs). The EOS card is located adjacent to the R5 module,  
58 but the cooling pipes (without electrical breaks) run directly underneath it without a shared heat path, in  
59 contrast to the barrel EOS. The remaining module and petal core design details are largely identical to the  
60 barrel module description above. Fig. 2 depicts the geometry of the endcap petal.

Figure 2: Endcap strip geometry

61    1.2. Radiation environment

62    A key input to the calculation is the radiation environment of the strip system, as several inputs depend  
 63    on radiation damage effects. The sensor leakage current can be parametrized as a function of the fluence  
 64    expressed in 1 MeV neutron-equivalents, and the TID effect on the digital chip current will be described as  
 65    a function of the total ionizing dose rate (more details on its dependencies can be found in Section 7).

66    Predictions for both of these parameters for each point in the ITk are available which have been generated  
 67    using the FLUKA particle transport code and the PYTHIA8 event generator (Fig. 3) [4]. Both of these  
 68    distributions display a weak dependence on  $z$  in the barrel, whereas they vary significantly along  $r$  and  $z$   
 69    over the length of the endcap petals. Because of this, and the linear uniformity of the stave compared to  
 70    the more complex geometry along a petal, we modelled only two types of modules for the barrel (a generic  
 71    module along the linear part of the stave and the module next to the end-of-structure card), but six different  
 72    types of modules in a petal.

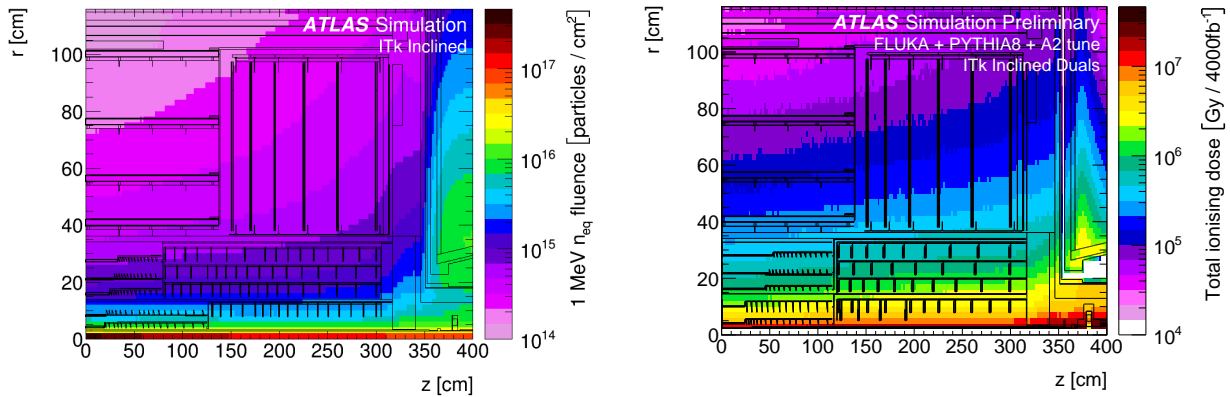


Figure 3: ATLAS ITk radiation environment. 1 MeV neutron equivalent fluence (left) and total ionizing dose (right). Both plots are for an integrated luminosity of  $4000 \text{ fb}^{-1}$  [4].

73    2. The electrical model

74    *From Graham: I think there is too much detail here (although it is doubtless accurate). Could the text be  
 75    simplified, given that information is available in figure 4?*

76    The electrical model consists of low-voltage (LV) and high-voltage (HV) circuits, depicted in Fig. 4.  
 77    The LV current is used to power the hybrid controller chips (HCCs), ATLAS Binary Chips (ABCs) and  
 78    Autonomous Monitoring and Control chip (AMAC) located on PCBs that are glued directly onto the surface  
 79    of the sensor. The number of chips vary according to the design of each different module type (barrel  
 80    short-strip and long-strip modules, and six different endcap module designs).

81    The ABCs and HCCs are all powered at 1.5 V using a DCDC converter (the FEAST) to step the voltage  
 82    down from 11 V (linPOL12V and bPOL12V in Fig. 4). Typically one FEAST per module is used to power  
 83    the chips; however, due to the large number of ABCs on endcap module R3, the load is split across two  
 84    FEAST converters on the module.

85    The AMAC contains a component powered at 1.5 V and one powered at 3 V; both are delivered from  
 86    the 11V source by an LDO regulator with a 1.9 mA quiescent current. Again, the endcap module R3 differs  
 87    from other modules, containing two AMACs each powered by its own LDO.

88    The bus tape, which carries both LV and HV currents, has a small wire resistance, which impacts the  
 89    module in two ways. First, the tape itself will generate some heat according to the amount of current passing  
 90    through it; this source of heat is accounted for in the model, however the contribution to the total module  
 91    power is negligible. Second, the voltage supplied to the module reduces slightly with distance from the EOS  
 92    end of the barrel stave or endcap petal. The treatment of this effect is slightly different in the barrel and  
 93    endcap models: in the barrel, the voltage delivered to every module is set at 10.5 V; in the endcap, the  $\Delta V$

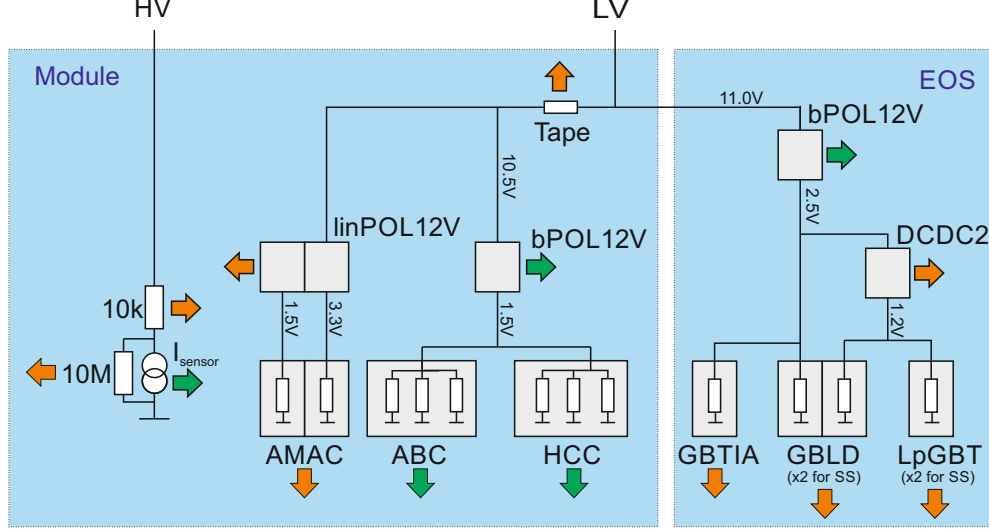


Figure 4: The electrical model of the ITk Strip barrel and endcap modules. Green arrows represent temperature-dependent heat sources, while orange arrows are temperature-independent. Grey squares are chips. Chip counts per module are linPOL12V/bPOL12V/AMAC: 1 each (2 each for EC R3); HCC: 1 for barrel LS, 2 for barrel SS and EC R0-R2 and R4-R5, 4 for EC R3; ABC: barrel: 10, 20 (LS, SS), EC: 17, 21, 21, 28, 16, 18 (R0-R5).

is estimated based on the calculated expected power loss along the tape for each module. In both cases, the impact of using a different treatment is small.

The low-voltage current is also delivered to the EOS card to power various data transfer components, which require 2.5 V and 1.2 V supplies. On the EOS, a FEAST identical to the one used on the module is used to step the voltage down from 11 V to 2.5 V; an additional LDO regulator brings the 2.5 V down to 1.2 V for some components. The EOS cards on the endcap petals and the long-strip staves have one GBLD and one LpGBT; EOS cards on the short-strip staves contain two of each. All EOS cards contain one GBTIA.

*Comment from Graham: I think that if we are going to refer to GBLD, LpGBT etc. then there should be a short sentence that describes (in a word) what each of these chips does?*

Finally, the HV current provides the voltage bias on the silicon sensors. An HV multiplexer switch (HVMUX) is placed in parallel to the sensor, which can be used to disconnect the sensor from the bias line requiring a parallel resistor in order to function. Two HV filters with an effective resistance of 10 kΩ are placed in series with the sensor. The nominal operating voltage of the sensor is expected to be 500V, but the system is designed to operate with a voltage bias of up to 700V.

### 3. The thermal model

The thermal network consists of heat sources (some of which are temperature dependent) and thermal resistances. The latter are given by the properties of the mechanical design (heat conductivities of the materials) and the geometry of the heat path. The geometry is generally 3-dimensional, but it is the strategy of the simple network models to lump the 3-dimensional behaviour into one thermal resistance parameter. In the models discussed here we have used a granularity corresponding to single detector modules for which the thermal resistance has been modelled. The temperatures in the model are then given for the nodes in the network in analogy to the potentials in an electrical network.<sup>2</sup>

The complexity of the thermal network used in this study (see Fig. 5) is given by the variety of different temperature-dependent heat sources in the ATLAS strip system. These sources consist of the digital power

<sup>2</sup>Historically Fourier's description of heat conduction pre-dated and inspired Ohm's work on electrical resistive networks. Here we follow the opposite direction.

118 for each type of chip, the heat generated by the FEAST chip providing the on-detector DC-DC conversion,  
 119 and the sensor leakage currents. In the ATLAS ITk strip modules all of these components are located on top  
 120 of the sensors, such that the heat generated in them flows through the sensor into the support structure, the  
 121 stave (barrel) or petal (endcap) core with the embedded cooling pipe. In the network model, the heat flow  
 122 from these sources is combined and flowing through a common impedance  $R_M$  to the sink at a temperature  
 123  $T_C$ . For each of the temperature-dependent heat sources (ABC, HCC, FEAST and the sensor) we have added  
 124 a resistance from the common temperature  $T_{mod}$  to allow for a finite and different heat path for each of them.  
 125 Finally, the End-of-substructure (EOS) card adjacent to the last module on the barrel stave (endcap petal)  
 126 is modeled as an additional source of heat with an independent impedance for its unique thermal path.

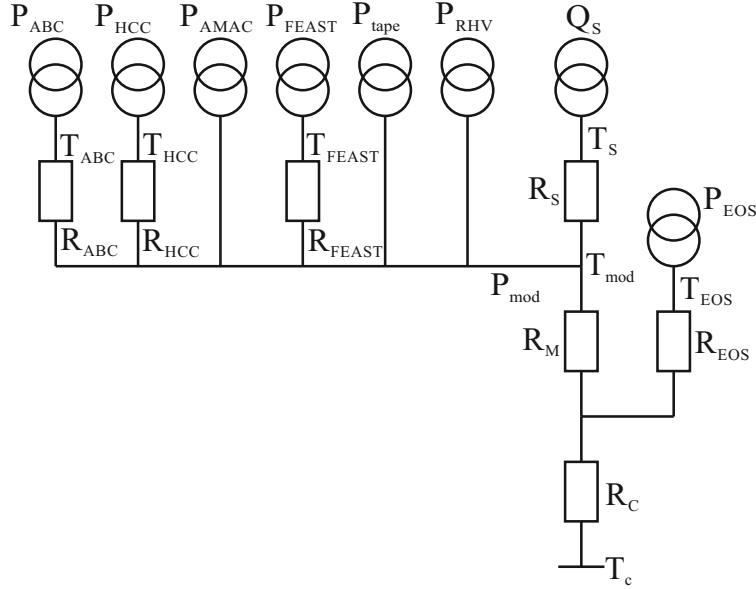


Figure 5: Thermal network model.

127 This is a more complex thermal network than the one studied in Ref. [3], where an analytical solution  
 128 for the determination of thermal stability was given. In particular, because of the non-linear temperature  
 129 dependence of some of the heat sources, it is not possible in this case to solve the set of equations describing  
 130 the model analytically. However, the set of equations is still sufficiently small to solve numerically using  
 131 functional programming languages such as Mathematica (used in the barrel model) or Python (used in the  
 132 endcap system).

#### 133 4. Obtaining thermal impedances using FEA

134 *(This section should be discussed and agreed between Graham and Yu-Heng)*

135 The cooling path between the sources dissipating electrical power and the cooling fluid is three-dimensional  
 136 and includes components with orthotropic thermal conductivity. Hence the prediction of temperature at any  
 137 node of the model requires a 3d thermal FEA Ref [Abaqus, Ansys]. However, the thermal conductivities of  
 138 the components along the path are approximately constant, so that the temperature rise above the coolant  
 139 temperature of any node  $i$  ( $i = \text{ABC, HCC, AMAC, FEAST, tape, RHV, or sensor}$ ) of the structure,  
 140  $\Delta T_i \equiv T_i - T_c$ , in the thermal network model is adequately described by a linear sum of contributions from  
 141 individual sources, i.e:

$$\Delta T_i = R_i P_i + (R_C + R_M) \sum_j P_j, \quad (2)$$

142 where we have momentarily ignored the EOS contribution.

143 In order to extract the thermal impedances for the thermal network model the finite element model is run  
 144 multiple times, with each heat source (or group of similar sources) switched on in turn with a representative  
 145 amount of heat. For each of these cases the temperature of all nodes in the thermal network model (Figure 5)  
 146 are calculated. The temperature of a node is here taken as the average of the temperatures for all the  
 147 gridpoints in the FEA model within the volume of the object corresponding to the node<sup>3</sup>. The thermal  
 148 impedances are then obtained from a fit of eq. 2 using the temperature data for all nodes for all cases of heat  
 149 injection.

150 Because of the nature of the network the fitted value for the common impedance  $R_{CM} = R_C + R_M$  is  
 151 dominated by the observed temperature rises of components where no heat is injected. The linearity of  
 152 this relationship is illustrated in fig. 6. The values for the additional component-specific impedances are in  
 153 turn driven by the observed temperature rise in the component with the heat injected in that particular  
 154 component.

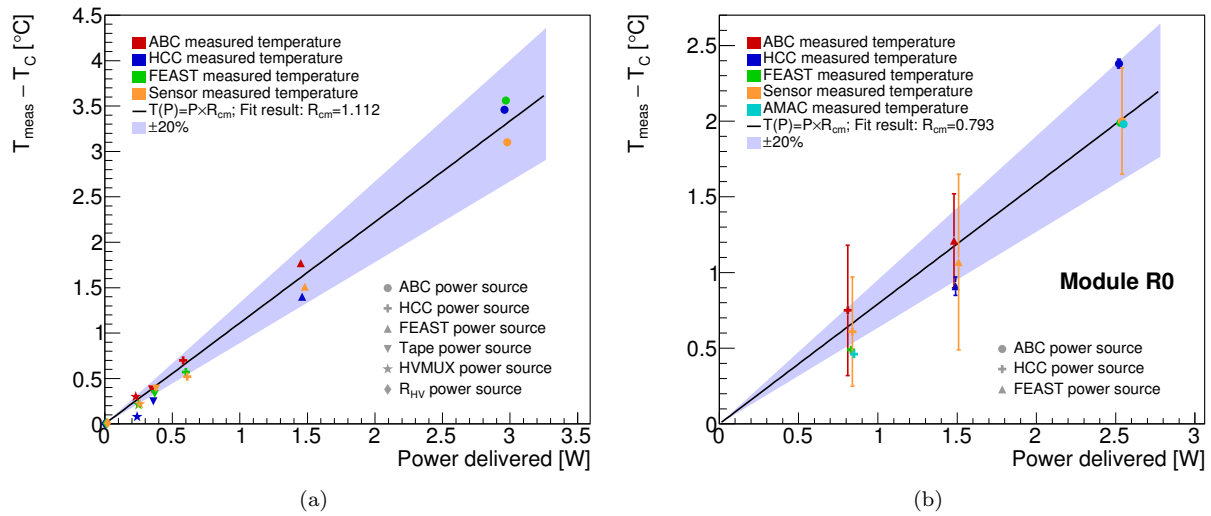


Figure 6: The relationship between the temperature rise observed in the FEA for a specific component vs the heat injected in another component. The slope of the fitted line is the estimate for  $R_{CM}$ . (a) The fit for a short-strip barrel module adjacent to the EOS. (b) The fit for the endcap R<sub>0</sub> module. For each data point marker, the source of power is indicated by the shape, and the measured component is indicated by the color. In (b), the error bars represent the standard deviation of temperatures of that particular component, and are not considered in the fit. The blue band represents a ±20% error band on the fit for  $R_{CM}$ .

155 For a barrel module the agreement of the network temperatures using the thermal impedances from the  
 156 fit with the data from FEA is better than 0.5°C for all nodes. This procedure is performed for both, the  
 157 EOS and the normal module. The thermal impedance from the sensor to the sink ( $R_M + T_C$ ) in all cases is  
 158 between 1.1 and 1.4 °C/W, but higher values (between 10 and 20 °C/W) are found for other impedances in  
 159 the network ( $R_{HCC}$  and  $R_{FEAST}$ ), mostly because these are for components with a small footprint constituting  
 160 a bottleneck for the heat flow.

161 There are two recognised departures from linearity of the thermal path: the rise in thermal conductivity  
 162 of the silicon sensor with decreasing temperature and the rise in heat transfer coefficient (HTC) to the  
 163 evaporating CO<sub>2</sub> coolant with increasing thermal flux. The FEA models are run using mean values for these  
 164 quantities appropriate to the operating conditions, and the thermoelectric model results are insensitive to

<sup>3</sup>This is particularly interesting in the case of the sensor, which fills a large volume, with a potentially large range of temperatures. Ref. [3] is not clear about the exact definition of the sensor temperature to be used for the calculation of the thermal impedance. In fact, at the time we were still using the maximum sensor temperature for the calculation of thermal stability. Since then we have acquired more experience with thermal network models and found that the best agreement is achieved if the average sensor temperature is used.

165 the variations expected in practice.

166 [GAB: Should we expand on this with plots and tables? There are detailed differences between stave and  
167 petal that might be confusing, e.g. re coefficients for the sensor T. Maybe all we could addin the end is  
168 confusion! ].

## 169 5. Other model inputs

170 The two temperature-dependent elements of the thermoelectric model—the radiation-induced digital cur-  
171 rent increase in the front-end chips, and the efficiency of the FEAST DCDC converter—are described in  
172 this section. Both effects are studied experimentally and fit with functional forms in order to accurately  
173 represent them in the model. The uncertainty in the experimental data, and in our modeling assumptions,  
174 are estimated here and considered in the evaluation of safety factors, described in detail in Section 7.2.

### 175 5.0.1. DCDC converter

176 The DCDC converter (FEAST) supplies a low-voltage (1.5 V) current to the ABC130 and HCC front-  
177 end chips on the module. The efficiency of the FEAST depends on its temperature as well as the output  
178 (load) current load delivered to the front-end chips. To correctly model the FEAST efficiency, experimental  
179 measurements have been performed to characterize the dependence and fitted with a functional form.

180 To measure the FEAST efficiency, the FEAST power board was glued to an aluminum cold plate, cooled  
181 with CO<sub>2</sub>, and powered with the nominal working input and output voltages (11 V input, 1.5 V output).  
182 The temperature of the FEAST was measured with an NTC thermistor and PTAT sensor residing on the  
183 FEAST, for a range of load currents up to the maximum design current of 4A<sup>4</sup>.

184 The data was then fit with a function with sufficient parameters to ensure reasonable agreement; the  
185 choice of functional form has no physical interpretation. Figure 7 depicts the FEAST efficiency data and  
186 the parameterized fit used in the model. The parameterization fits the data with an accuracy below 1%;  
187 this uncertainty in the FEAST efficiency modeling is small compared to other uncertainty sources, and is  
188 therefore neglected in our model.

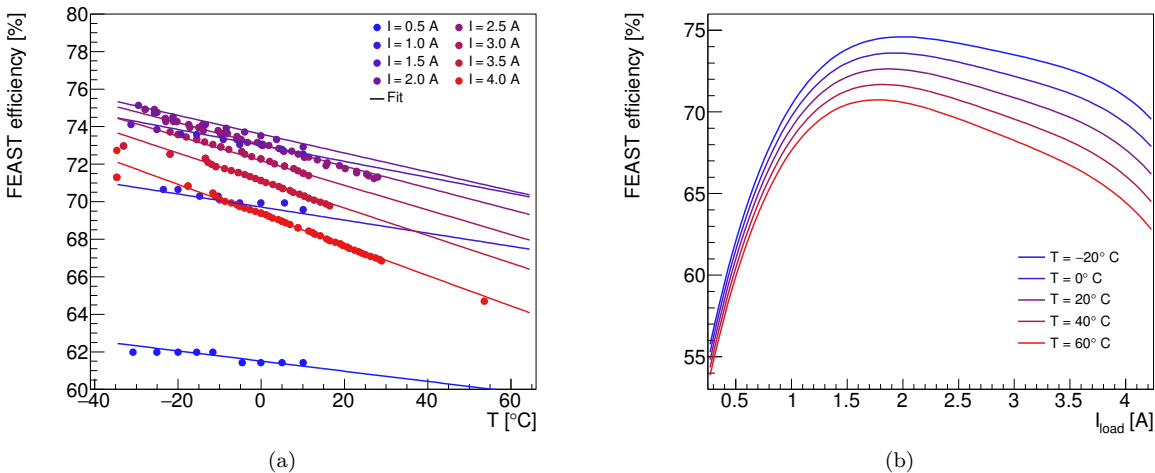


Figure 7: The FEAST efficiency model based on experimental data. (a) The experimental data points characterizing the FEAST efficiency are plotted as dots and color coded for load current. The data is compared to the analytic fit, evaluated in curves of equal current. (b) The same analytic fit, presented as a function of current load for curves of equal temperature.

<sup>4</sup> FEAST data spreadsheet: [http://project-dcdc.web.cern.ch/project-dcdc/public/Documents/FEASTMod\\_Datasheet.pdf](http://project-dcdc.web.cern.ch/project-dcdc/public/Documents/FEASTMod_Datasheet.pdf). Cite?

189 5.0.2. Digital current increase of chips using 130 nm CMOS technology

190 The ABC and HCC chips, designed using IBM 130 nm CMOS8RF technology, are known to suffer from an  
 191 increase in digital current when subjected to a high-radiation environment [1]. This phenomenon, known as  
 192 the “TID bump,” is well-studied [5, 6] and has a characteristic shape whereby the effect reaches a maximum  
 193 as a function of the accumulated dose and then gradually diminishes (see Fig. 8).

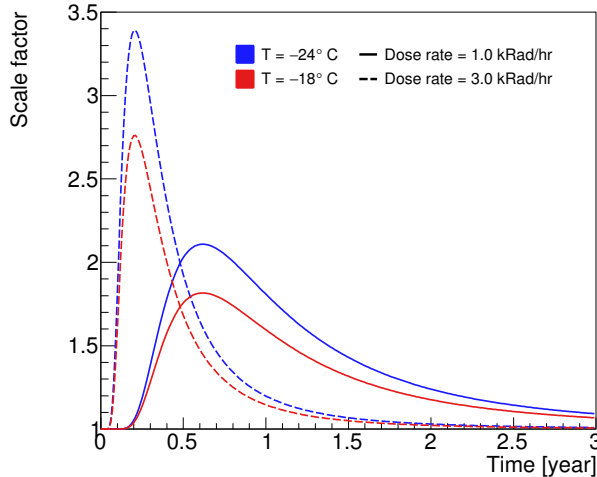


Figure 8: Parametrization of the impact of the total ionizing dose on the magnitude of the front-end chip digital current (the TID bump), presented as a function of time. The current is multiplied by a scale factor that is modeled as a function of total ionizing dose, dose rate, and temperature, based on experimental data.

194 In an effort to characterize the nature of the TID bump in the ABC and HCC chips empirically, many  
 195 irradiation campaigns have been conducted using a variety of radiation sources, testing the effect at different  
 196 temperatures and dose rates. The data collected from these studies was used to develop a model of the  
 197 TID bump that estimates the digital current increase given the total ionizing dose, the dose rate, and the  
 198 operating temperature of the chip. This parameterization, which is depicted in Fig 8, is used as an input to  
 199 the thermoelectric model in order to correctly model the ABC and HCC currents. The TID bump is assumed  
 200 to fully apply to the HCC digital current, and apply to 69% of the ABC digital current (according to our  
 201 understanding of its digital circuitry).

202 The TID bump displays certain key features, which are reflected in the parameterization: first, the effect  
 203 is larger at colder temperatures and higher dose rates. This means it can be mitigated by operating the  
 204 chips at higher temperature (note that the dose rate is fixed by the LHC conditions). Second, the figure  
 205 also illustrates how chips receiving different dose rates will reach their maximum digital current increase  
 206 at different times. This feature is particularly important when modeling the total power consumed by the  
 207 barrel and endcap systems. In both systems, the dose rate varies significantly depending on the position of  
 208 the module in the detector. The effect means that the maximum system power will be smaller than the sum  
 209 of the maximum power of each module, as each chip reaches its maximum at a different point in time.

210 The TID bump is an important source of uncertainty in our model. The experimental data suggests a  
 211 relatively large variation in the TID bump effect, in particular between different batches of the same type  
 212 of chip delivered by the manufacturer, suggesting an unknown effect in the fabrication process. To estimate  
 213 the uncertainty in the TID bump, the parameterized function is fit again using only the worst-performing  
 214 data (defined as having the largest TID bump effect). This “pessimistic” parameterization is used as a safety  
 215 factor to estimate the detector performance in worst-case scenarios.

216 The irradiations of individual chips have typically been performed at constant dose rate and temperature.  
 217 In our model calculations both of these parameters vary throughout the evaluation. In our parametrization  
 218 we use only the instantaneous value of these two parameters, thus neglecting any possible history of the  
 219 TID effect. We also ignore any short-time effects due to variations in the dose rate on the scale of hours  
 220 or days. This approach is mandated by the lack of more varied experimental data and the absence of a  
 221 good theoretical model for this effect. This probably constitutes the largest source of unknown errors for our

model.

### 5.0.3. Radiation-dependent leakage current

The radiation-induced leakage current can be parametrized as a function of the hadron fluence expressed in 1 MeV equivalent neutrons. The parametrizations we have used for the evaluation of our model are shown in Fig. 9 [ref Marcella Mikestikova]. The currents given there are at a sensor temperature of -15°C and are scaled in our model to the specific sensor temperature using eq. 1.

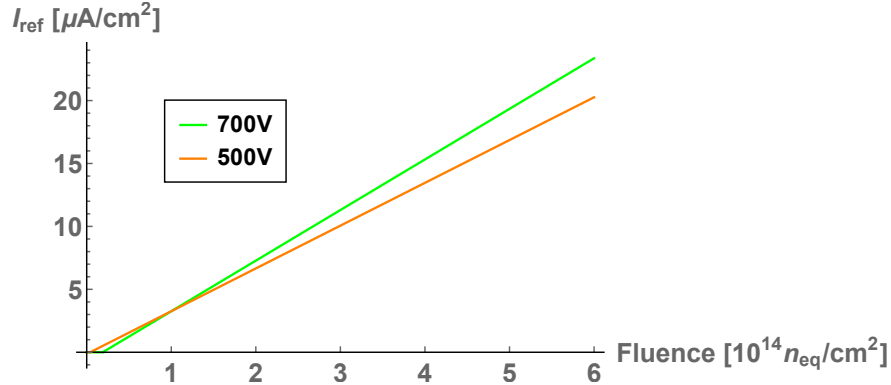


Figure 9: Parametrization used for the leakage current at -15°C as a function of the fluence for two different sensor bias voltages.

## 6. Running the model

The thermoelectric model constructs a profile of the sensor module operation conditions over the lifetime of the detector in the following manner. First, assuming a reasonable set of initial component temperatures, the module total power (including all components, but excluding the sensor leakage power) and the sensor temperature without leakage current ( $T_0$ ) is calculated assuming these initial temperatures. The initial value for the module power is used to solve for the sensor power and temperature accounting for leakage current, using the thermal balance equation and the relationship from Eq. 1. Using this calculated sensor leakage current and temperature, the power and temperature of the module components are updated given the initial (year 0, month 0) startup parameters.

Next, the module conditions of the following month (year 0, month 1) are calculated. Using the component temperatures calculated from the previous month and the operational parameters (ionizing dose and dose rates) from month 1, the module total power (excluding sensor leakage) is again calculated, and subsequently the sensor temperature and leakage current are computed. Following this, the module component temperatures and power values are derived for this month. This process is repeated in one-month steps until the final year of operation, or until a real solution for the sensor temperature does not exist, indicating that thermal runaway conditions have been reached.

In the barrel subsystem, the above procedure is performed four separate times to represent the radiation conditions of the four barrel layers located at different radii from the beam axis<sup>5</sup> for both, a module next to the EOS card (hereafter referred to as ‘EOS module’) and a module along the length of the stave away from the EOS card (‘normal module’). Thus in total, 8 modules are simulated for the barrel (4 layers  $\times$  normal/EOS), and they are combined in their proper proportion to simulate the entire barrel system.

In the endcap subsystem, the total ionizing dose and dose rates vary significantly depending on the position of the module; furthermore, the design of each module on a petal differs significantly. Therefore, all 36 module types (6 rings  $\times$  6 disks) are simulated independently, and combined to represent the full endcap.

<sup>5</sup>The correct module type, short-strip in the inner two layers and long-strip for the outer two layers, is used for each layer.

We have implemented this algorithm in Mathematica (barrel) and Python (endcaps). In both cases the calculation for a set of operating conditions over the full lifetime of the LHC takes between 5 and 10 minutes on a standard PC, thus enabling a quick turn-around for systematic studies of the parameter space.

## 7. Outputs of the thermoelectric model

### 7.1. Operational scenarios

To study the different aspects of our predictions for the operation of the ITk strip system throughout its lifetime, we performed the calculation of the system parameters over the expected 14 years of operation in monthly steps as outlined in section 6. Time-dependent inputs to the calculations were given from the expected performance of the LHC (Fig. 10a) and different profiles for the cooling temperature. We studied flat cooling temperature scenarios at different temperatures starting at  $-35^{\circ}\text{C}$ , the lowest evaporation temperature achievable with the ITk evaporative  $\text{CO}_2$  cooling system, and a ‘ramp’ scenario in which the cooling temperature starts at  $0^{\circ}\text{C}$  and gradually is lowered down to  $-35^{\circ}\text{C}$  over the course of 10 years (Fig. 10b).

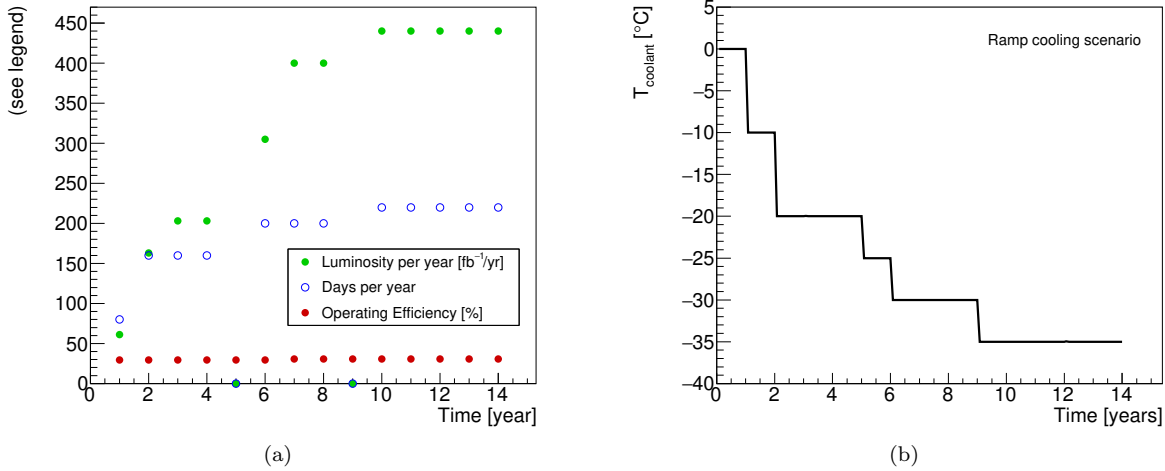


Figure 10: (a) Expected LHC performance and (b) ‘cooling ramp’ scenario for the coolant temperature. Year-long shutdowns of the LHC are anticipated in years 5 and 9.

### 7.2. Safety factors

To ensure the robustness of the system design against errors in the assumptions used in the model, we also evaluate the model using a set of input parameters with some key inputs degraded. The set of safety factors used is given in Table 1. Each safety factor has been estimated individually based on experience, the complexity of the system aspect described by the parameter, and from available data or the absence of such data. Note that the model can be evaluated with all the safety factors listed in Table 1 used together, a situation which is unlikely to occur in the real system, to provide a worst-case estimate for the performance of the ITk strip system. The individual effects of the different safety factors are demonstrated in figure 11.

### 7.3. Results

The thermo-electrical model provides a large range of predictions for the operation of the strip system. A detailed discussion of all results would only be of interest to ITk strip system experts and is beyond the scope of this article. Instead we will present here a subset of results to demonstrate the capabilities and use of the thermo-electrical model for the design of the detector system.

Table 1: Safety factors.

Safety factor on	Value	Reason
Fluence	50%	Accuracy of fluence calculations and uncertainties in material distributions
Thermal impedance	10% endcap, 20% petal	Local support build tolerances, thermal network assumptions
Digital current	20%	Final chip performance and parametrization of TID effect
Analog current	5%	Final chip performance
Tape electrical impedance	10%	Electrical tape manufacturing tolerances
Bias voltage	700 V	Increased bias voltage from nominal 500 V to maintain S/N
TID parametrization	Nominal/Pessimistic	Different data sets for fit of TID bump

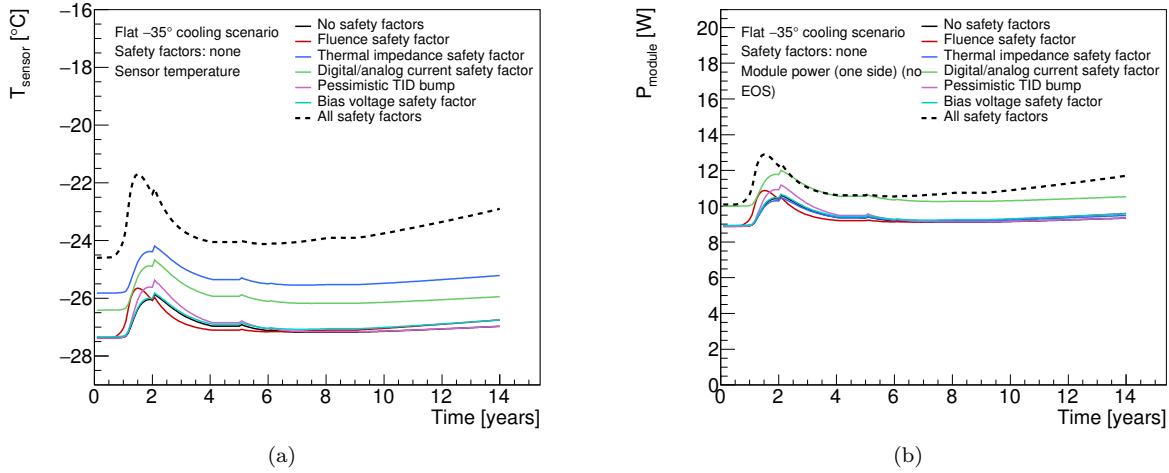


Figure 11: Comparing the impact of different safety factors on (a) the sensor temperature and (b) the module power for the R3 endcap module. The dotted line depicts the effect of all safety factors applied at once.

### 277 7.3.1. Module properties

Example output plots for module properties from the thermo-electrical modules are shown in Figures 12 and 13. The different radiation-dependent effects occur on different times scales. The maximum in the digital chip power due to the TID effect occurs relatively early (in year 1 to 4), although the bump has a long tail, particularly in the outer layers of the barrel. The sensor leakage power on the other hand grows towards the end of the lifetime of the ITk. If the leakage current would continue to increase in the case of further irradiation, or if the cooling temperature would be higher, this growth would ultimately lead to thermal runaway. Due to the radial dependence of the radiation environment, the radiation-induced effects are most pronounced in the innermost layers.

286 7.3.2. System properties

One of the key concerns for the design of the strip system is thermal stability of the system. If the cooling temperature is too high to limit the leakage power from the radiation-damaged sensors to a level where it can still be removed the system is unstable (it goes into ‘thermal runaway’). In this case there is no solution to the set of equations in the thermo-electrical model any more and the numerical search for a solution fails. In the barrel strip system this happens in the last year of operation at a cooling temperature of  $-15^{\circ}\text{C}$  under nominal conditions, and at  $-25^{\circ}\text{C}$  (in year 13) with safety factors applied. As the design cooling temperature of the ITk cooling system is  $-35^{\circ}\text{C}$  we have confidence that the ITk strip system has sufficient margin for thermal stability.

295 Beyond the issue of stability, the thermo-electrical model delivers predictions for the development of

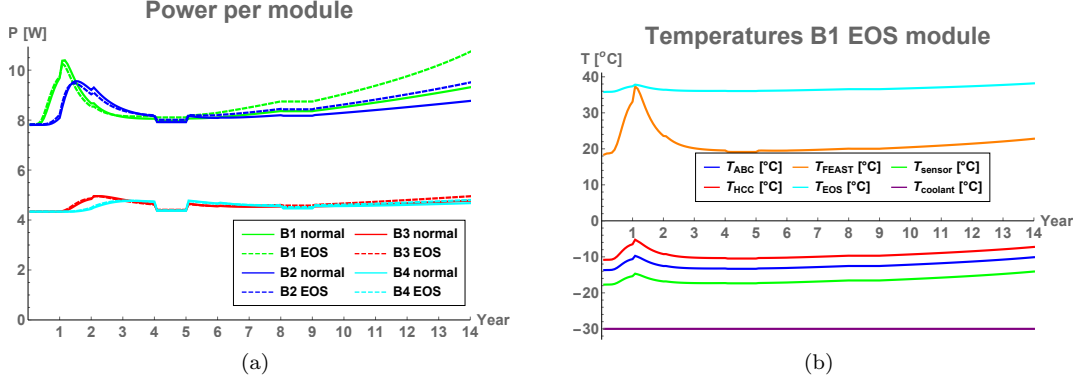


Figure 12: Examples of barrel module performance predictions for a flat cooling scenario ( $-30^\circ$ ) including safety factors. (a) Power per module. (b) Temperatures for different nodes of an end-of-stave barrel module in the innermost barrel.

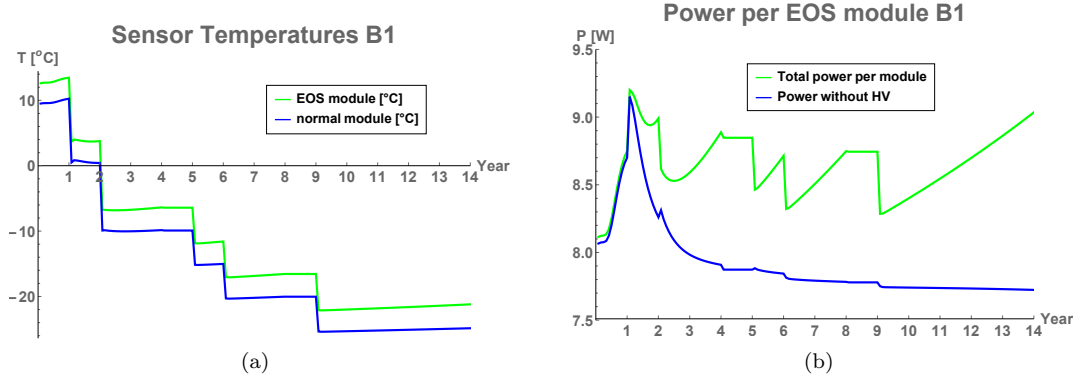


Figure 13: Examples of barrel module performance predictions for the ramp cooling scenario including safety factors. (a) Sensor temperature in the innermost barrel modules. (b) Power in an end-of-stave barrel module in the innermost layer.

296 current and power requirements for the overall system. Some of the predictions are shown in figure 14. Again,  
 297 the different timescales of the various radiation-induced effects are visible. Ignoring this time dependence could  
 298 lead to overspecification of some system aspects like the total cooling power.

299 These predictions are now used throughout the strip project to consistently size power supply and cooling  
 300 systems. Including safety factors in the predictions gives us some confidence that the designs are robust and  
 301 by using commonly agreed safety factors we ensure a consistent use of safety factors throughout the project  
 302 and prevent safety factor creep.

303 Because of the different timescales for the peak power due to the TID effect and the sensor leakage due  
 304 to radiation there is room for the optimization of the cooling temperature profile for minimal power. The  
 305 thermo-electrical model is a powerful tool to plan such an optimized cooling profile. In fact, the cooling  
 306 'ramp' scenario introduced in Section 7.1 is the result of such an optimization (Fig. 15).

## 307 8. Model performance verification

308 The quality of the predictions of the thermo-electrical model is affected by two major factors: First, there  
 309 is the quality of the input parameters, and second there are errors introduced by reducing the complex 3D  
 310 geometry into a linear thermal impedance network. The former have been discussed throughout this paper  
 311 where the different inputs have been presented. For the latter we have studied the agreement of predictions  
 312 from the network model with the more accurate results obtained from FEA for selected states of the system.

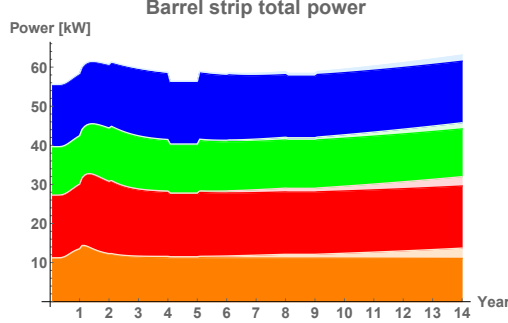


Figure 14: Examples for system performance predictions. Barrel total power requirements for flat -30° cooling including safety factors (left): The plot shows the stacked power requirements for the four barrels (orange: innermost barrel, blue: outermost barrel). Full colour indicates power from the front-end electronics, greyed parts are contributions from HV power for the four barrels.

For the verification of this agreement we have calculated the sensor temperature curve for a barrel end-of-stave module up to thermal runaway. For this we do not vary any of the input parameters in the model other than the sensor leakage power. We therefore can reduce the complex thermal network to its Thevenin equivalent, which is identical to the network studied in Ref. [3] and we can use the analytical expressions given there. The comparison of this prediction is shown in Fig. 16. Despite a large temperature variation of about 15°C across the sensor, which is caused by heat flux from the end-of-structure card and degraded thermal impedance at the end of the stave due to ceramic sections in the cooling pipe, the network model predicts the runaway within 1°C of the result from the FEA. This agreement gives us confidence that the use of a thermal network model is not likely to significantly degrade the predictions beyond the errors introduced by other inputs to the model.

## 9. Conclusions

We have developed a model of the ATLAS ITk strip system which is based on the interplay between a thermal and an electrical network model. The set of equations in the model can be numerically solved using standard data analysis software in short time, allowing for a quick turn-around for systematic studies of the system performance. The complexity of these networks is given by the number of interconnected components between the networks which have a non-linear dependence on the temperature or electrical power. This approach could easily be adopted for any other silicon detector system.

In the case of the ATLAS strip system several temperature-dependent heat sources had to be included. In addition to the sensor leakage current these are the radiation-induced increase of the digital front-end power ('TID bump') and the efficiency of the DC/DC conversion system. The outputs of the model give us confidence that the ITk strip system will be thermally stable until the end of LHC phase II operation even if safety factors on key inputs are included. The model furthermore provides information for benchmark system parameters like cooling and supply power and currents in power cables, which is used in the specification of these systems. The use of the model outputs throughout the strip project ensures consistent specifications, including a common strategy on safety factors. Using the thermo-electrical model we can also propose an optimized cooling temperature 'ramp' scenario, which equalizes leakage power throughout the lifetime of the experiment while minimizing the TID bump.

We have verified the performance of the thermal network model compared to full FEA and are confident that the agreement is sufficient that the overall accuracy of the model is dominated by other inputs to the model, of which the most likely source of unknown error are limitations in the parametrization of the TID effect available for the model.

## 10. Acknowledgements

The evaluation of the termo-electrical model depends critically on the input parameters to the model. To capture the whole of the system these need to distill all what is known of the system, and we are therefore

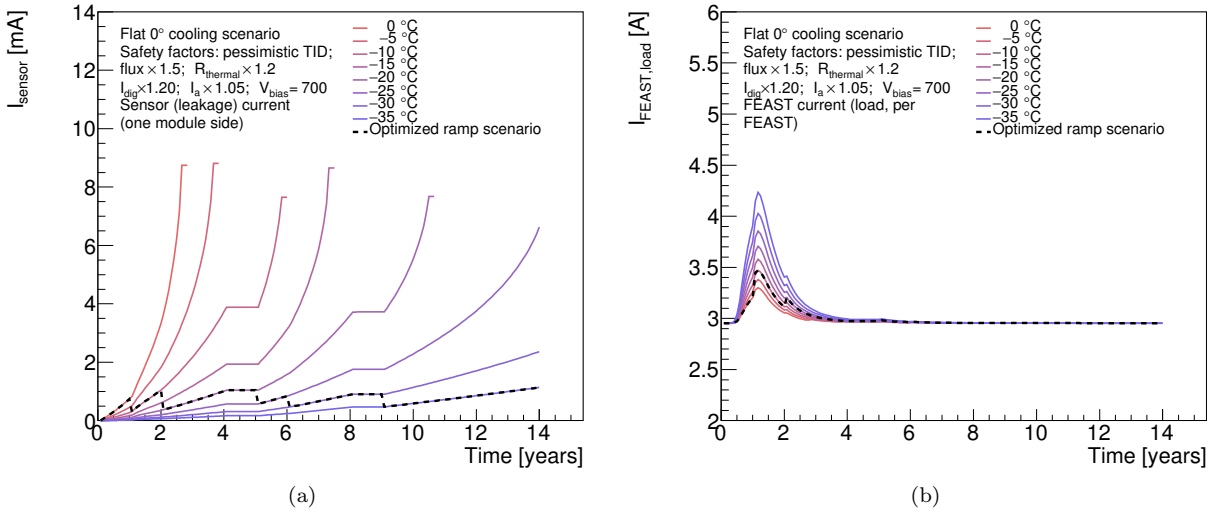


Figure 15: Performance of the cooling ‘ramp’ scenario specified in Fig. 10b. The dashed lines represents the ramp scenario, which has been selected so that the sensor leakage current (a) is stable throughout the lifetime of the ITk. A higher coolant temperature in the first few years reduces the TID effect, keeping the current load on the FEAST (b) well below its specified maximum of 4 A.

347 indebted to the whole of the ITk strip community. In particular we would like to thank Tony Affolder, Kyle  
 348 Cormier, Ian Dawson, Sergio Diez Cornell, Laura Gonella, Ashley Greenall, Alex Grillo, Paul Keener, Steve  
 349 McMahon, Paul Miyagawa, Craig Sawyer, Francis Ward and Tony Weidberg for all their inputs to this work.

## 350 References

- 351 [1] ATLAS Collaboration, Technical Design Report for the ATLAS Inner Tracker Strip Detector.
- 352 [2] Radiation induced effects in the ATLAS Insertable B-Layer readout chip, Tech. Rep. ATL-INDET-PUB-  
 353 2017-001, CERN, Geneva (Nov 2017).  
 354 URL <https://cds.cern.ch/record/2291800>
- 355 [3] G. Beck, G. Viehhauser, Analytic model of thermal runaway in silicon detectors, Nucl. Instrum. Meth.  
 356 A618 (2010) 131–138. doi:[10.1016/j.nima.2010.02.264](https://doi.org/10.1016/j.nima.2010.02.264).
- 357 [4] Atlas experiment - radiation simulation public results [cited 2018-11-17].  
 358 URL <https://twiki.cern.ch/twiki/bin/view/AtlasPublic/RadiationSimulationPublicResults#FLUKA%20Simulations>:
- 360 [5] F. Faccio, G. Cervelli, Radiation-induced edge effects in deep submicron cmos transistors, IEEE Trans-  
 361 actions on Nuclear Science 52 (6) (2005) 2413–2420. doi:[10.1109/TNS.2005.860698](https://doi.org/10.1109/TNS.2005.860698).
- 362 [6] F. Faccio, H. J. Barnaby, X. J. Chen, D. M. Fleetwood, L. Gonella, M. McLain, R. D. Schrimpf, Total  
 363 ionizing dose effects in shallow trench isolation oxides, Microelectronics Reliability 48 (7) (2008) 1000  
 364 – 1007, 2007 Reliability of Compound Semiconductors (ROCS) Workshop. doi:<https://doi.org/10.1016/j.microrel.2008.04.004>.  
 365 URL <http://www.sciencedirect.com/science/article/pii/S0026271408000826>

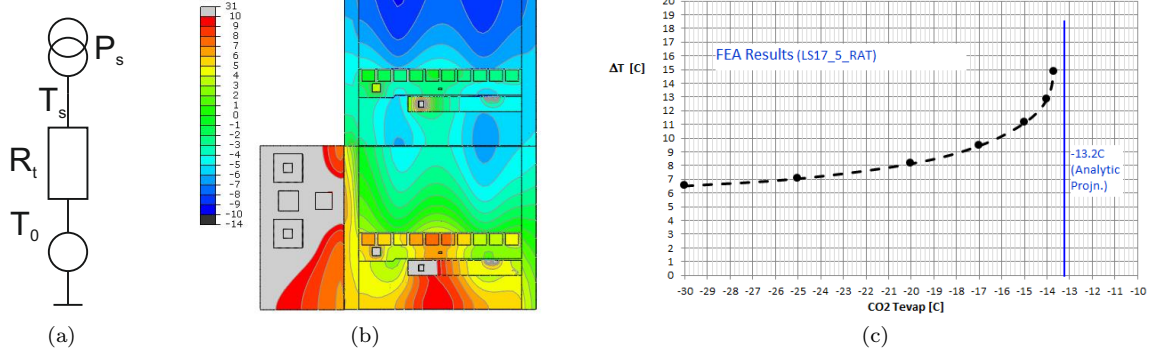


Figure 16: (a) Thevenin equivalent of the thermal network. (b) Result of surface temperature calculations using FEA. (c) Average temperature above cooling, comparing FEA (dots) and the network model prediction (dotted line).